2nd Symposium on New Trends in Nuclear and Medical Physics, Poland, September 24–26, 2025

Monte Carlo Assessment of Entanglement-Based Positron Emission Tomography

K. Nakamura[a,*], P. Caradonna[b], M. Fujimoto[c], M. Uenomachi[d] and K. Shimazoe[b,c]

[a]*Department of Systems Innovation, School of Engineering, The University of Tokyo, Bunkyo-ku, Tokyo 113-8656, Japan*
[b]*Department of Nuclear Engineering and Management, Graduate School of Engineering, The University of Tokyo, Bunkyo-ku, Tokyo 113-8656, Japan*
[c]*Department of Bioengineering, Graduate School of Engineering, The University of Tokyo, Bunkyo-ku, Tokyo 113-8656, Japan*
[d]*Institute of Science Tokyo, 2-12-1 Ookayama, Meguro-ku, 152-8550 Tokyo, Japan*

Doi: 10.12693/APhysPolA.148.S138 *e-mail: nakamura-koki0626@g.ecc.u-tokyo.ac.jp

Monte Carlo simulations were conducted to evaluate the coincidence selection performance in the conventional and Compton-based positron emission tomography systems under identical geometric and activity conditions. A ring detector composed of eight 8×8 Ce:GAGG crystal array modules was modeled using the Geant4 toolkit, with annihilation events generated to mimic fluorine-18 decay. Two performance metrics were examined, i.e., the relative true event detection efficiency and the true event fraction (both computed as functions of the coincidence time window). The Compton configuration yielded fewer total true coincidences than conventional positron emission tomography but achieved a consistently higher true event fraction, indicating improved rejection of random and scattered events. Simulations performed for low- and high-activity conditions, incorporating both entangled and non-entangled annihilation photon states, showed that entanglement further enhanced the true event fraction, particularly at lower activity, where accidental coincidences were less dominant. The enhancement observed at $A \approx 0.167$ GBq corresponded to only a few percent increase in true event fraction, but the effect was systematic across the tested coincidence windows. These findings demonstrate that coincidence selection using quantum polarization correlations can enhance selection fidelity under relaxed timing conditions and suggest a potential pathway toward more timing-tolerant positron emission tomography architectures.

topics: positron emission tomography (PET), Compton scattering, quantum entanglement, Monte Carlo methods

1. Introduction

Positron emission tomography (PET) is an imaging modality that plays a central role in clinical diagnostics and preclinical research [1–3]. By detecting pairs of 511 keV photons from positron–electron annihilation, PET provides functional images of biological processes. The spatial resolution and quantitative accuracy of these images are strongly influenced by the method used to select coincident photon pairs. Conventional PET systems rely on coincidence timing and energy windows to identify photon pairs, but finite window widths make them susceptible to accidental coincidences and scattered events, which degrade image quality [4, 5]. Increasing the width of these windows improves event statistics by including more true coincidences, but it also introduces additional random and scattered events; conversely, narrower windows reduce noise at the cost of lower sensitivity.

These trade-offs highlight the need for new discrimination methods that can extend coincidence selection beyond conventional timing and energy criteria. To address these challenges, the use of quantum correlations between annihilation photons, an approach referred to as quantum-entangled positron emission tomography (QEPET), is under investigation both theoretically [6–10] and experimentally [11–18].

In this study, we present a direct comparison of the true event fraction (TEF) achievable with conventional PET and QEPET using the Geant4 simulation toolkit [19, 20]. A compact, ring-shaped

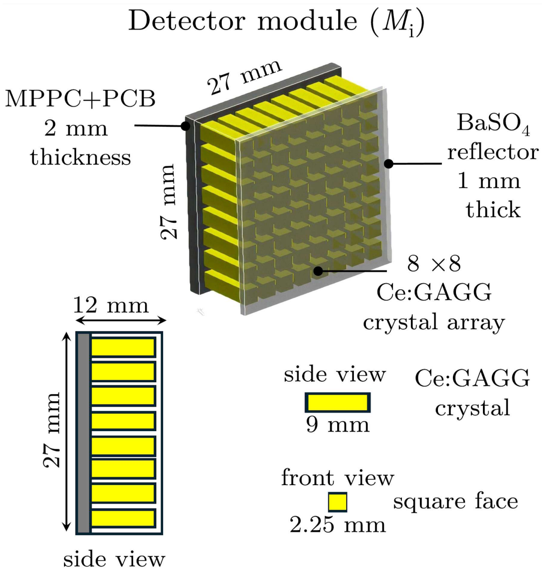

Fig. 1. Schematic of a single detector module composed of an 8×8 array of cerium-doped GAGG (Ce:GAGG) crystals optically coupled to a multi-pixel photon counter mounted on a printed circuit board (MPPC + PCB), together with a $BaSO_4$ reflector plate. This module is one of eight forming the simulated ring detector (see Fig. 2).

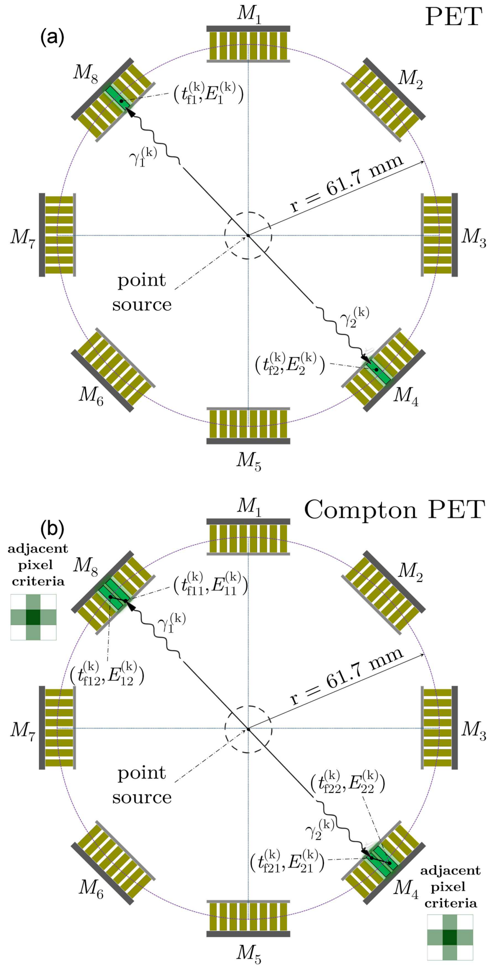

Fig. 2. Schematic illustrations of the coincidence pair construction for (a) conventional PET and (b) Compton PET systems. Panel (a) shows the eight-module detector ring, indicating the locations where photon detection times and deposited energies are recorded for conventional coincidence selection. Panel (b) illustrates the Compton PET configuration, in which each annihilation photon undergoes two successive interactions (Compton scatter and absorption) within separate crystals, resulting in four time-correlated detections as described in the text.

detector system was simulated to generate annihilation events representative of fluorine-18 decay. The TEF of both systems was evaluated as a function of the coincidence time window to determine whether entanglement-based polarization correlations can improve the identification of true coincidences.

2. Method

2.1. Detector model and simulation setup

Monte Carlo simulations were performed using the GEANT4 toolkit (version 10.6.2) [19–21]. To isolate the effects of coincidence selection, the detector-level energy and timing resolutions were not included (i.e., no Gaussian smearing was applied to the deposited energies or hit times).

The simulated detectors replicated the design reported by Kim et al. [12]. For this reason, only a brief summary is provided here.

The system consists of a ring detector comprising eight identical modules. Each module includes a 2 mm-thick multi-pixel photon counter and printed circuit board (MPPC + PCB) assembly, a scintillator layer containing an 8×8 array of cerium-doped gadolinium aluminum gallium garnet (Ce:GAGG) crystals, and a 1 mm-thick $BaSO_4$ reflector, as illustrated in Fig. 1. Figure 2 shows the complete simulated ring detector with eight modules arranged on a mean radius of $r = 61.7$ mm.

The positron–electron annihilation events, resulting in the production of photon pairs with an energy of 511 keV, were simulated at the center of the ring detector under atmospheric conditions. Each event emitted two photons in opposite directions along random radial axes, with polarization states entangled in orthogonal correlation. The detector modules were treated as having ideal energy and spatial resolution.

To emulate positron sources of different activities, two source intensities were considered. The lower-activity case corresponded to approximately $A \approx 0.167$ GBq, while the higher-activity case corresponded to approximately $A \approx 1.67$ GBq.

These activities were derived from a total of 10^9 simulated annihilation events divided by the respective acquisition windows $W = 6$ s and $W = 0.6$ s, assuming constant activity within each interval. The relationship between the simulated activity and the acquisition window was therefore defined as

$$A = \frac{10^9}{W}, \tag{1}$$

where A is the average decay rate in becquerels [Bq].

The timestamps of events generated by the simulation were shifted in time by an offset denoted t_s, sampled from an exponential decay distribution, representing the radioactive decay law. The decay constant was defined as

$$\lambda = \frac{\ln(2)}{T_{1/2}}, \tag{2}$$

where the half-life of fluorine-18, $T_{1/2} = 109.8$ min, was used as a representative isotope commonly employed in PET imaging.

Since radioactive decay follows an exponential law, for each annihilation event k, the offset time t_s was sampled from a truncated exponential distribution $\exp(\lambda)$ within the interval $[0, W]$. The maximum cumulative probability of this distribution was

$$P_{\max} = 1 - \mathrm{e}^{-\lambda W}, \tag{3}$$

which defines the upper limit of the truncated range. For each annihilation event k, a uniform random number u_k was generated within the range $[0, P_{\max})$, and the inverse transform method was applied to compute

$$t_s^{(k)} = -\frac{1}{\lambda} \ln(1 - u_k). \tag{4}$$

This method guarantees that each generated time shift $t_s^{(k)}$ satisfies the condition $0 \le t_s^{(k)} \le W$, ensuring that the random emission time assigned to each photon lies within the observation period and corresponds to the instant at which the photon would have been emitted in the simulated decay. The higher-activity case ($A \approx 1.67$ GBq) corresponds to the shorter acquisition window ($W = 0.6$ s) and thus a higher instantaneous decay rate, while the lower-activity case ($A \approx 0.167$ GBq) corresponds to the longer window ($W = 6$ s).

For each scintillation hit k belonging to an accepted event, the final timestamp $t_{fi}^{(k)}$ was defined as

$$t_{fi}^{(k)} = t_s^{(k)} + t_i^{(k)}, \tag{5}$$

where $t_i^{(k)}$ is the time provided by the simulation, representing the photon time of flight from the annihilation origin to the Ce:GAGG crystal hit position. No detector-level timing smearing was applied, so $t_{fi}^{(k)}$ corresponds to the ideal detection time in the simulation.

The higher-activity configuration ($A \approx 1.67$ GBq) produced a higher instantaneous event rate, thereby increasing the probability of accidental coincidences relative to the lower-activity configuration ($A \approx 0.167$ GBq). The resulting set of final timestamps $t_{fi}^{(k)}$ was used as the basis for all coincidence selections and analyses described in the following sections.

2.2. Conventional coincidence selection scheme

We first consider the conventional coincidence pair detection scheme used in PET systems, as illustrated in Fig. 2a. Each annihilation event k generates a pair of photons, labeled $\gamma_1^{(k)}$ and $\gamma_2^{(k)}$, which are emitted from the center of the detector ring and detected, for example, by modules M_4 and M_8 at times $t_{f1}^{(k)}$ and $t_{f2}^{(k)}$, respectively.

An event is accepted as a coincidence when the absolute difference between the two detection times is smaller than the coincidence time window Δt, i.e.,

$$\left| t_{f1}^{(k)} - t_{f2}^{(k)} \right| < \Delta t, \tag{6}$$

provided that the detections occur in different modules ($M_a \neq M_b$) and that the registered photon energies satisfy

$$E_1^{(k)} = E_2^{(k)} = 511 \text{ keV} \pm 51.1 \text{ keV}. \tag{7}$$

A pair is classified as *true* if and only if $\gamma_1^{(k)}$ and $\gamma_2^{(k)}$ originate from the same annihilation event, as illustrated in Fig. 2a.

2.3. Compton PET coincidence selection scheme

In a Compton camera-based PET system, we consider the case in which each annihilation photon undergoes two successive interactions within a detector module — first a Compton scatter and then a photoelectric absorption, yielding four time-correlated detections per event within the coincidence window Δt (Fig. 2b). For photon $\gamma_1^{(k)}$ detected in module M_8, the recorded interaction times are $t_{f11}^{(k)}$ and $t_{f12}^{(k)}$, while for photon $\gamma_2^{(k)}$ detected in module M_4, the times are $t_{f21}^{(k)}$ and $t_{f22}^{(k)}$. The index $j = 1, 2$ in $t_{fij}^{(k)}$ labels the first and second interactions, respectively.

The timing differences between the two crystal interactions in each module are

$$\left| t_{f11}^{(k)} - t_{f12}^{(k)} \right| = \Delta t_{M_8}, \qquad \left| t_{f21}^{(k)} - t_{f22}^{(k)} \right| = \Delta t_{M_4}, \tag{8}$$

where only horizontally or vertically adjacent crystal pairs were included in the analysis. Diagonal neighbors were excluded (see Fig. 3).

An energy constraint was applied in each module ($M_a \neq M_b$), yielding

$$E_{i0}^{(k)} = E_{fi1}^{(k)} + E_{fi2}^{(k)} = 511 \text{ keV} \pm 51.1 \text{ keV} \tag{9}$$

(for $i = 1, 2$), with $E_{i0}^{(k)}$ being the total deposited energy for annihilation photon γ_i.

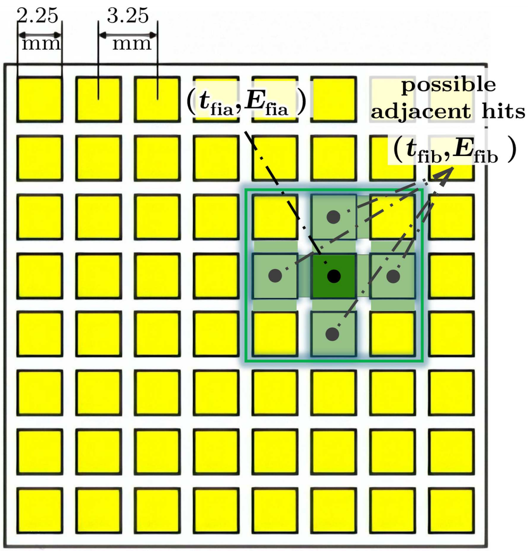

Fig. 3. Front view of the Ce:GAGG crystal array in a detector module. A coincidence pair can form only between crystals that are directly adjacent horizontally or vertically; diagonal neighbors are excluded.

To compare arrival times between modules, each photon is assigned an average detection time, i.e.,

$$\tau_{f1}^{(k)} = \frac{t_{f11}^{(k)} + t_{f12}^{(k)}}{2}, \qquad \tau_{f2}^{(k)} = \frac{t_{f21}^{(k)} + t_{f22}^{(k)}}{2}. \tag{10}$$

The difference between these average times defines

$$\left|\tau_{f1}^{(k)} - \tau_{f2}^{(k)}\right| = \Delta t_{M_{(4-8)}}, \tag{11}$$

where $\Delta t_{M_{(4-8)}}$ serves the same role in Compton PET as the coincidence time condition defined in (6) for conventional PET.

All timing gates were set equal, i.e.,

$$\Delta t_{M_4} = \Delta t_{M_8} = \Delta t_{M_{(4-8)}} = \Delta t, \tag{12}$$

so that a single coincidence window Δt governs all timing comparisons between and within modules, enabling a direct assessment of random-coincidence effects under consistent conditions.

2.4. Interaction sequence determination

We adopted the definition of the relative azimuthal angle $|\Delta\Phi|$ between the scattering planes of $\gamma_1^{(k)}$ and $\gamma_2^{(k)}$ as given by Kim et al. [12]. This angle characterizes the relative orientation between the two Compton-scattering planes originating from the same annihilation event.

To tailor selection to this simulation, only events with $85^\circ \le |\Delta\Phi| \le 95^\circ$ were accepted, and both photons were required to satisfy $70^\circ \le \theta \le 121^\circ$.

Detector modules cannot determine the order of two interactions occurring within the same module, so both possible sequences were evaluated for a two-hit crystal pair (a, b) with deposited energies $E_{fia}^{(k)}$ and $E_{fib}^{(k)}$. For the sequence hypothesis $a \mapsto b$,

$$\cos\left(\theta_{ia}^{(k)}\right) = 1 - mc^2 \left(\frac{1}{E_{ia}^{\prime(k)}} - \frac{1}{E_{i0}^{(k)}}\right), \tag{13}$$

where $mc^2 = 511$ keV, $E_{ia}^{\prime(k)} = E_{i0}^{(k)} - E_{fia}^{(k)}$ is the kinetic energy of the photon scattered from crystal a, and $E_{i0}^{(k)} = E_{fia}^{(k)} + E_{fib}^{(k)}$, consistent with (9). The reversed ordering $b \mapsto a$ gives

$$\cos\left(\theta_{ib}^{(k)}\right) = 1 - mc^2 \left(\frac{1}{E_{ib}^{\prime(k)}} - \frac{1}{E_{i0}^{(k)}}\right), \tag{14}$$

where $E_{ib}^{\prime(k)} = E_{i0}^{(k)} - E_{fib}^{(k)}$ is the kinetic energy of the photon scattered from crystal b.

Although each photon in the simulation possesses a definite linear polarization, the ensemble is statistically unpolarized because the polarization directions are randomly distributed in azimuth. Consequently, the polarization-averaged Klein–Nishina kernel was used to estimate the relative sequence probabilities between the two possible interaction orderings.

If exactly one of the angles $\theta_{ia}^{(k)}$ or $\theta_{ib}^{(k)}$ lies within the range $70^\circ \le \theta \le 121^\circ$, then this sequence is selected. If both scattering angles satisfy this condition, the relative probabilities are evaluated as

$$\mathrm{Prob}(a\mapsto b) \propto \left(\frac{E_{ia}^{\prime(k)}}{E_{i0}^{(k)}}\right)^2 \left[\frac{E_{ia}^{\prime(k)}}{E_{i0}^{(k)}} + \frac{E_{i0}^{(k)}}{E_{ia}^{\prime(k)}} - \sin^2\left(\theta_{ia}^{(k)}\right)\right],$$

$$\mathrm{Prob}(b\mapsto a) \propto \left(\frac{E_{ib}^{\prime(k)}}{E_{i0}^{(k)}}\right)^2 \left[\frac{E_{ib}^{\prime(k)}}{E_{i0}^{(k)}} + \frac{E_{i0}^{(k)}}{E_{ib}^{\prime(k)}} - \sin^2\left(\theta_{ib}^{(k)}\right)\right], \tag{15}$$

and cases yielding equal probabilities are rejected.

3. Results

3.1. Detection efficiency comparison

To establish a baseline comparison between the conventional PET and Compton PET systems described in Sect. 2 and illustrated in Fig. 2, the relative true event detection efficiency was introduced as a performance metric. This quantity expresses the ratio of the effective rates at which the two systems successfully detect and accept true coincidence pairs.

The relative efficiency η_{rel} [in %] is defined as the ratio of the total number of accepted registered events (true plus background) in a Compton PET system, N^{cpet}, to that number in the conventional PET system, N^{pet}, i.e.,

$$\eta_{\mathrm{rel}}(\Delta t) = \frac{N^{\mathrm{cpet}}(\Delta t)}{N^{\mathrm{pet}}(\Delta t)} \times 100. \tag{16}$$

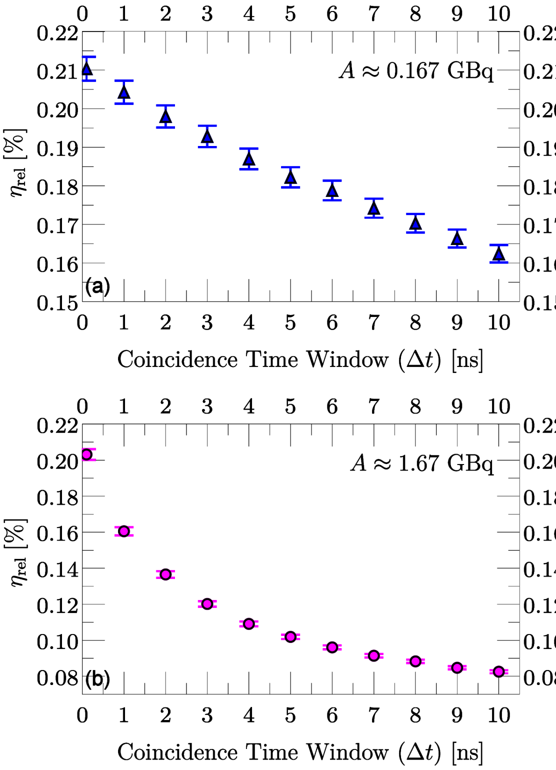

Fig. 4. Relative true event detection efficiency η_{rel} (in percent) between Compton PET and conventional PET as a function of the coincidence time window Δt for (a) $A \approx 0.167$ GBq and (b) $A \approx 1.67$ GBq. In both cases, $\eta_{\mathrm{rel}} < 100\%$ and decreases monotonically with increasing Δt, indicating lower true event detection efficiency for the Compton PET configuration.

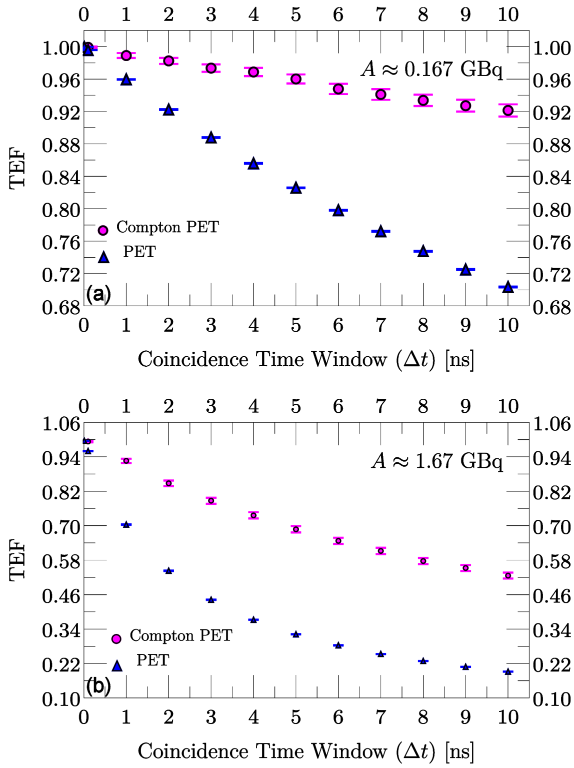

Fig. 5. True event fraction (TEF) as a function of the coincidence time window Δt for the PET configuration (shown in Fig. 2a) and the Compton PET configuration (shown in Fig. 2b). Case (a) $A \approx 0.167$ GBq, and case (b) $A \approx 1.67$ GBq.

This metric provides a direct measure of the relative detection capability introduced by the Compton-based coincidence logic, independent of geometry or source intensity. Values of $\eta_{\mathrm{rel}} < 100\%$ indicate that the Compton PET configuration yields fewer accepted true coincidences than the conventional PET system, whereas $\eta_{\mathrm{rel}} > 100\%$ would correspond to a net gain in detection efficiency.

Figure 4a and b shows the variation of η_{rel} with the coincidence time window Δt for activities of approximately $A \approx 0.167$ GBq and $A \approx 1.67$ GBq, respectively. In both cases, η_{rel} remains below 0.22% across the entire range $0 \leq \Delta t \leq 10$ ns, indicating that the Compton PET configuration yields fewer accepted true coincidences than the conventional PET system under identical conditions.

For the lower-activity case ($A \approx 0.167$ GBq), η_{rel} appears to decrease linearly from approximately 0.21% to 0.16% while Δt increases from 0 to 10 ns. In contrast, for the higher-activity case ($A \approx 1.67$ GBq), the relative efficiency exhibits a broader variation, decreasing monotonically in a nonlinear fashion from about 0.20% to 0.08%. The consistently decreasing trend in both cases reflects the growing contribution of accidental coincidences at larger Δt, which disproportionately affects the Compton PET scheme.

3.2. True event fraction between PET and Compton PET

The true event fraction quantifies the proportion of detected coincidences that correspond to true annihilation events as opposed to background coincidences. It is defined as

$$\mathrm{TEF}(\Delta t) = \frac{N_{\mathrm{true}}(\Delta t)}{N_{\mathrm{true}}(\Delta t) + N_{\mathrm{bg}}(\Delta t)}, \tag{17}$$

where $N_{\mathrm{true}}(\Delta t)$ denotes the number of true coincidence events and $N_{\mathrm{bg}}(\Delta t)$ denotes the number of background coincidences. The definition of $N_{\mathrm{true}}(\Delta t)$ follows that of the previous subsection, with the superscript identifying the PET configuration omitted for clarity.

The true event fraction (TEF) obtained for both PET and Compton PET configurations shown in Fig. 2 is presented in Fig. 5 for simulated source activities of $A \approx 0.167$ GBq and $A \approx 1.67$ GBq.

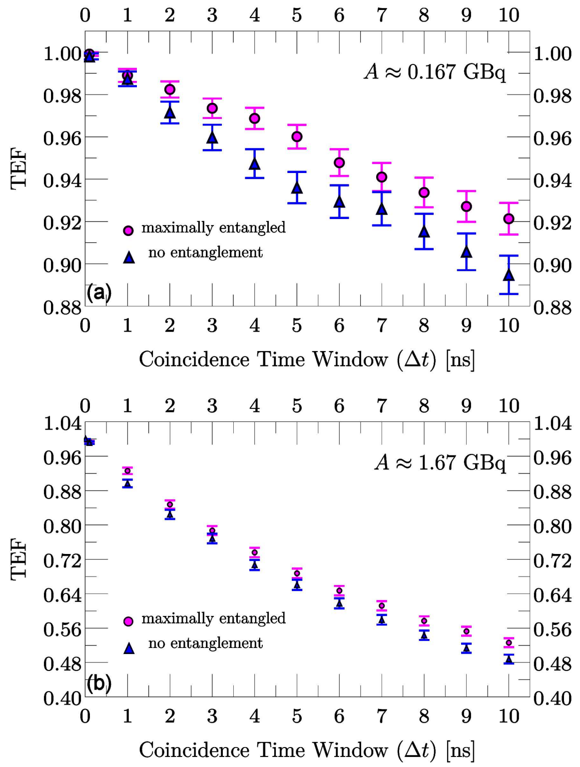

Fig. 6. True event fraction as a function of the coincidence time window Δt for Compton PET simulations performed with (a) $A \approx 0.167$ GBq and (b) $A \approx 1.67$ GBq. Each panel compares maximally entangled and Bohm–Aharonov mixed (non-entangled) states. In both cases, the entangled configuration yields higher TEF, with the relative enhancement more pronounced at lower activity.

In both configurations, TEF decreases as the coincidence time window Δt widens, reflecting the increasing inclusion of random background events. At the lower activity of $A \approx 0.167$ GBq (Fig. 5a), Compton PET maintains a TEF above 92% across the examined range, while the TEF in conventional PET is more sensitive to Δt, reaching a minimum of about 70% at $\Delta t = 10$ ns.

For the higher simulated activity $A \approx 1.67$ GBq (Fig. 5b), both PET configurations exhibit lower TEF values than in the low-activity case ($A \approx 0.167$ GBq), because the higher count rate increases the number of accidental coincidences. At low activity, Compton PET maintains a TEF value between 0.92 and 1.00 across the full coincidence window range $0 \leq t \leq 10$ ns, whereas conventional PET spans from 0.70 to 1.00. At high activity, the TEF of Compton PET decreases to approximately 0.48–1.00, while that of conventional PET drops further to about 0.15–1.00. These results show that although TEF decreases for both systems as activity rises, Compton PET remains more resilient to accidental coincidences and consistently preserves a higher fraction of true events across all activity levels and timing conditions.

3.3. Influence of photon entanglement on the true event fraction

In 1957, Bohm and Aharonov [22] proposed a quantum mechanical reference model for annihilation photons that preserves the same marginal polarization distributions and rotational invariance as the maximally entangled state, but lacks off-diagonal coherence (i.e., it is a mixed, non-entangled state) [7]. The purpose of this reference model is to provide a classical polarization benchmark; measured cross sections that exceed this baseline indicate nonclassical, entanglement-driven correlations.

Based on the geometry shown in Fig. 2b, the TEF was computed from (17) as a function of Δt for both the maximally entangled and Bohm–Aharonov mixed states at $A \approx 0.167$ GBq and $A \approx 1.67$ GBq.

For $A \approx 0.167$ GBq (Fig. 6a), a measurable TEF enhancement is observed with entanglement, and the curves diverge with increasing Δt. For $A \approx 1.67$ GBq (Fig. 6b), the same qualitative behavior appears, though the relative enhancement is smaller, consistent with higher accidental rates at higher event densities.

4. Conclusions

This study used detailed Monte Carlo simulations to compare coincidence selection in conventional PET and Compton PET under identical geometric and activity conditions. Two quantitative metrics were analyzed, i.e., the relative efficiencies of detecting true events and true event fraction (TEF), which allows for a direct assessment of configuration differences and the influence of photon entanglement.

Compton PET records fewer total true coincidences than conventional PET, but yields a higher TEF across all tested coincidence windows. This indicates stronger rejection of random and scattered coincidences, particularly at wider timing gates where conventional PET performance degrades.

Comparing the entanglement-correlated photon pairs with a standard mixed state, we found that the entangled configuration exhibits a measurable enhancement in TEF. At lower activity ($A \approx 0.167$ GBq), the ratio of entangled to non-entangled TEF increases from approximately 1.00 at $\Delta t = 0.1$ ns to about 1.03 at $\Delta t = 10$ ns, corresponding to an enhancement of roughly one to three percent across the examined range. The difference diminishes at higher activity, where accidental coincidences become dominant, but the entangled configuration remains systematically higher across all tested conditions.

Overall, coincidence selection criteria using quantum polarization correlations can maintain the purity of selection under relaxed timing conditions.

Within the limits of the idealized model (no detector resolution or pile-up), these results suggest that timing-tolerant architectures could be feasible. Future work incorporating detector effects and experimental validation will determine how much of the enhancement persists under realistic operating conditions.

Acknowledgments

This work was supported by the Japan Society for the Promotion of Science (JSPS) KAKENHI under Grant No. 22H05022.

References

[1] M.E. Phelps, *Proc. Natl. Acad. Sci.* **97**, 9226 (2000).

[2] A.K. Shukla, U. Kumar, *J. Med. Phys.* **31**, 13 (2006).

[3] K. Lameka, M.D. Farwell, M. Ichise, in: *Handbook of Clinical Neurology* Vol. 135, Elsevier, 2016, p. 209.

[4] E.J. Hoffman, S.-C. Huang, M.E. Phelps, D.E. Kuhl, *J. Comput. Assist. Tomogr.* **5**, 391 (1981).

[5] T.J. Holmes, D.L. Snyder, D.C. Ficke, *IEEE Trans. Med. imaging* **3**, 68 (2007).

[6] P. Moskal, D. Kisielewska, C. Curceanu et al., *Phys. Med. Biol.* **64**, 055017 (2019).

[7] P. Caradonna, I. D'Amico, D.G. Jenkins, D.P. Watts, *Phys. Rev. A* **109**, 033719 (2024).

[8] P. Caradonna, *Ann. Phys.* **470**, 169779 (2024).

[9] P. Caradonna, *Phys. Rev. A* **111**, 053708 (2025).

[10] P. Caradonna, K. Shimazoe, *Phys. Rev. A* **112**, 032413 (2025).

[11] D. Watts, J. Bordes, J. Brown, A. Cherlin, R. Newton, J. Allison, M. Bashkanov, N. Efthimiou, N. Zachariou, *Nat. Commun.* **12**, 2646 (2021).

[12] D. Kim, A. N. Rachman, U. Taisei, M. Uenomachi, K. Shimazoe, H. Takahashi, *J. Instrum.* **18**, P07007 (2023).

[13] G. Romanchek, G. Shoop, S. Abbaszadeh, *Bio-Algorithms Med-Syst.* **19**, 9 (2023).

[14] H. Eslami, M. Mohamadian, *Eur. Phys. J. Plus* **139**, 976 (2024).

[15] P. Moskal, *Physics* **17**, 138 (2024).

[16] G.R. Romanchek, G. Shoop, M.A. Kupinski, P.H. Kuo, M. King, L.R. Furenlid, S. Abbaszadeh, *Bio-Algorithms Med-Syst.* **20**, 27 (2024).

[17] P. Moskal, D. Kumar, S. Sharma et al., *Sci. Adv.* **11**, eads3046 (2025).

[18] A.M. Kožuljević, T. Bokulić, D. Grošev, S. Parashari, L. Pavelić, M. Rade, M. Žuvić, M. Makek arXiv:2510.11504 (2025).

[19] J. Allison, K. Amako, J. Apostolakis et al., *IEEE Trans. Nucl. Sci.* **53**, 270 (2006).

[20] J. Allison, K. Amako, J. Apostolakis et al., *Nucl. Instrum. Methods Phys. Res. A* **835**, 186 (2016).

[21] S. Agostinelli, J. Allison, K. Amako et al., *Nucl. Instrum. Methods Phys. Res. A* **506**, 250 (2003).

[22] D. Bohm, Y. Aharonov, *Phys. Rev.* **108**, 1070 (1957).